www.acsnano.org

Solvation Structure of Methanol-in-Salt Electrolyte Revealed by Small-Angle X-ray Scattering and Simulations

Xingyi Lyu,[+] Haimeng Wang,[+] Xinyi Liu, Lilin He, Changwoo Do, Soenke Seifert, Randall E. Winans, Lei Cheng,* and Tao Li*

Cite This: *ACS Nano* 2024, 18, 7037−7045

Read Online

ACCESS | Metrics & More | Article Recommendations | Supporting Information

ABSTRACT: The solvation structure of water-in-salt electrolytes was thoroughly studied, and two competing structures—anion solvated structure and anion network—were well-defined in recent publications. To further reveal the solvation structure in those highly concentrated electrolytes, particularly the influence of solvent, methanol was chosen as the solvent for this proposed study. In this work, small-angle X-ray scattering, small-angle neutron scattering, Fourier-transform infrared spectroscopy, and Raman spectroscopy were utilized to obtain the global and local structural information. With the concentration increment, the anion network formed by $TFSI^-$ became the dominant structure. Meanwhile, the hydrogen bonds among methanol were interrupted by the $TFSI^-$ anion and formed a new connection with them. Molecular dynamic simulations with two different force fields (GAFF and OPLS-AA) are tested, and GAFF agreed with synchrotron small-angle X-ray scattering/wide-angle X-ray scattering (SAXS/WAXS) results well and provided insightful information about molecular/ion scale solvation structure. This article not only deepens the understanding of the solvation structure in highly concentrated solutions, but more importantly, it provides additional strong evidence for utilizing SAXS/WAXS to validate molecular dynamics simulations.

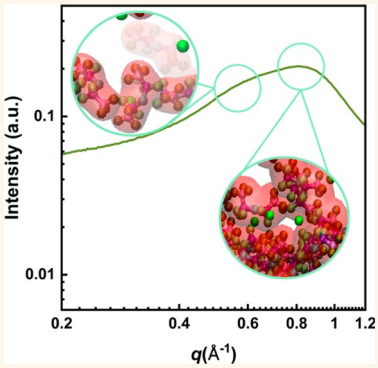

KEYWORDS: *Small-angle X-ray scattering, Small-angle neutron scattering, Fourier-transform infrared spectroscopy, Molecular dynamic simulation, Solvation structure*

INTRODUCTION

Considerable advantages were found for water-in-salt electrolytes (WISE) compared with the commercial organic electrolytes after introduced by Suo and his colleagues: nonflammable, nonvolatile, low toxicity, and wider electrochemical window.[1−4] Following this premier work, a fair amount of studies with multiple advanced techniques, such as Raman spectroscopy and infrared spectroscopy (IR), have been reported to explore the solvation structure of the WISE.[5−17] The anion coordination mode for imide-based electrolyte was commonly investigated by deconvoluting the Raman peak (S−N−S bending vibration) into three bands, which correspond to solvent-separated ion pair (SSIP), contact ion pair (CIP), and aggregate (AGG), respectively.[18−21] By analyzing the shift of infrared peaks caused by the vibration of the hydrogen−oxygen bond or deuterium-oxygen bond, the bulk-like and ion-bound water were found to coexist in the system and serve different roles as a medium for lithium ion transport and a lubricant, respectively.[6,9,22,23]

However, Raman spectroscopy and IR could not provide the global solvation structure. Recently, we used synchrotron small-angle X-ray scattering/wide-angle X-ray scattering (SAXS/WAXS), a powerful tool to provide structural information at the nanometer scale, to explore the solvation structure of the WISE at a larger scale.[8,24−26] In lithium bis(trifluoromethane sulfonyl)imide (LiTFSI) and water with a wide range concentration (from 1 to 20 mmol/g), two competing solvation structures presented by two peaks have been identified. The peak located at relatively lower q values (around 0.3−0.5 $Å^{-1}$) has been recognized as the $TFSI^-$ anion solvated structure (ASS), and a higher q value peak (around 1 $Å^{-1}$) was defined as the $TFSI^-$ anion network (AN),[27] where q

Received: October 24, 2023
Revised: January 18, 2024
Accepted: January 19, 2024
Published: February 19, 2024

https://doi.org/10.1021/acsnano.3c10469
ACS Nano 2024, 18, 7037−7045

is the scattering vetor ($q = (4\pi \sin(\theta)/\lambda$, where θ is related with scattering angle, and λ is the wavelength of X-ray).[24] As described in Scheme 1, with the concentration increment, the distance between the $TFSI^-$ anions becomes closer, and the $TFSI^-$ anion solvated structure diminishes in the system. Meanwhile, the $TFSI^-$ anion network begins to build and eventually dominates. A similar SAXS/WAXS pattern was also reported in the ionic liquids.[28−31] They assigned the peak centered at ~1 $Å^{-1}$ as a charge-ordering peak (COP), which is an extended electrostatic network formed by ions and their counterions.[28] We initially hypothesized that a higher q value peak (around 1 $Å^{-1}$) would be in the same category as the ionic liquid. However, further discovery pointed in another direction. The influence of cations on the $TFSI^-$ anion network is nearly nonexistent when using NaTFSI. In other words, the peak position remained unchanged. Additionally, the size calculated from the SAXS/WAXS profile is larger than that from the pure $TFSI^-$ itself. The aforementioned findings lead us to believe that the high q peak is caused not by COP but by interfacial water. Furthermore, we extended the work to other imide-based lithium salts with different symmetric fluorocarbon chain anions. Lithium bis(fluoro sulfonyl)imide (LiFSI), lithium bis(pentafluoroethane sulfonyl) imide (LiBETI), and lithium bis(nonafluorobutane sulfonyl)imide (LiBNTI) were studied with the same protocol as for LiTFSI.[32] The average distances ($d_{spacing}$) of anion solvated structure conform to a positive linear relationship with the carbon number of fluorocarbon chains, thus further confirming our hypothesis.[32]

Scheme 1. Change of Anion Solvated Structure (ASS) and Anion Network (AN) with Increament of LiTFSI[a]

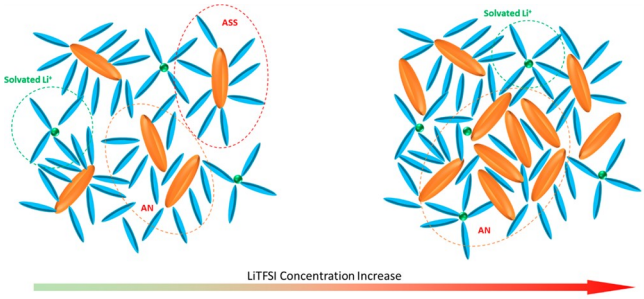

[a]The orange ellipsoid is $TFSI^-$ anion, blue ellipsoid is water molecule, and the green sphere is Li^+ ion.

After the effects of cations and anions are understood, the role of the solvent is the current focus to complete the puzzle. Methanol was chosen for this proposed study because it can be simply regarded as a hydrogen atom of water replaced with a methyl group. By introducing a methyl group, a system is established that maintains a certain relationship with the aqueous system. This choice would be able to facilitate us to find the universality of previously drawn conclusion. Meanwhile, methanol has been employed as a cost-effective additive to enhance the performance of Zn batteries,[33,34] and its direct utilization as a solvent has also been reported.[35] Therefore, SAXS/WAXS, FTIR, and Raman spectroscopy were utilized to explore the solvation structure of this methanol-in-salt electrolyte, combined and supported by molecular dynamics (MD) simulations. Like the WISE system, the $TFSI^-$ anion solvated structures and $TFSI^-$ anion networks were observed in SAXS/WAXS with two peaks at lower and higher q values. Free methanol and interfacial methanol were able to be determined by the FTIR. With the increment of concentration, more methanol was able to contact with $TFSI^-$ anions and become interfacial methanol. The methanol solution's $d_{spacing}$ of the $TFSI^-$ anion network is larger than that of WISE's because methanol is larger than water, which further confirms the high q peak is not from the charge-ordering. MD simulation also confirmed the shifts of the two peaks related to the concentration.

RESULTS AND DISCUSSION

As previously reported, SAXS/WAXS emerged as a valuable technique for probing the arrangement of anions of electrolytes on the nanometer scale.[8,27,32,36−39] In the same vein as the aqueous system (Figure 1a), SAXS/WAXS profiles for LiTFSI's methanol solutions with a broad range of concentrations have been obtained (Figure 1b). Two peaks were observed, and the peak assignment followed the principles established for the aqueous system.[27,32,36] The peak at the lower q region (peak MA) was assigned to the ASS, which means the average distance ($d_{spacing}$) between $TFSI^-$ anions. The peak at the higher q region (peak MB) was considered to represent the AN, where a narrow channel is formed by the gaps of the crowded $TFSI^-$ anions. The average distance between the solvated anions and the channel size

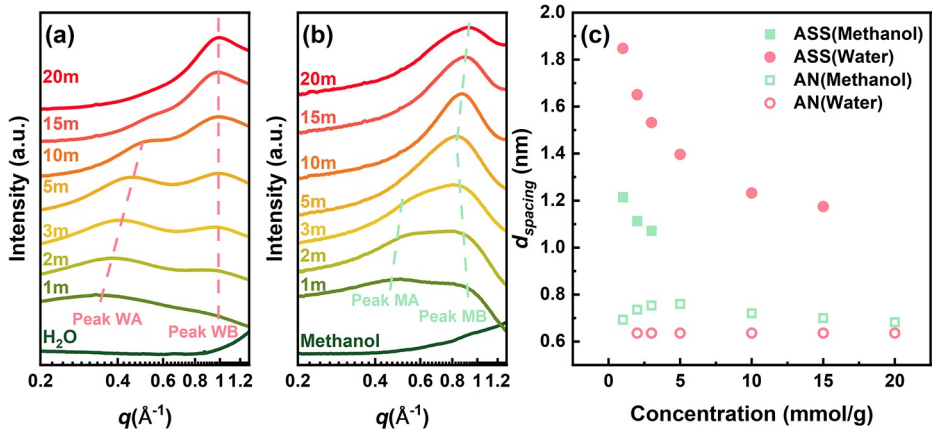

Figure 1. SAXS/WAXS profile for (a) water-in-LiTFSI electrolyte and (b) Methanol -in-LiTFSI electrolyte; (c) Statistics and comparison for $d_{spacing}$ of the anion-solvated-structure (ASS) and anion network (AN) from experiment and simulation.

https://doi.org/10.1021/acsnano.3c10469
ACS Nano 2024, 18, 7037−7045

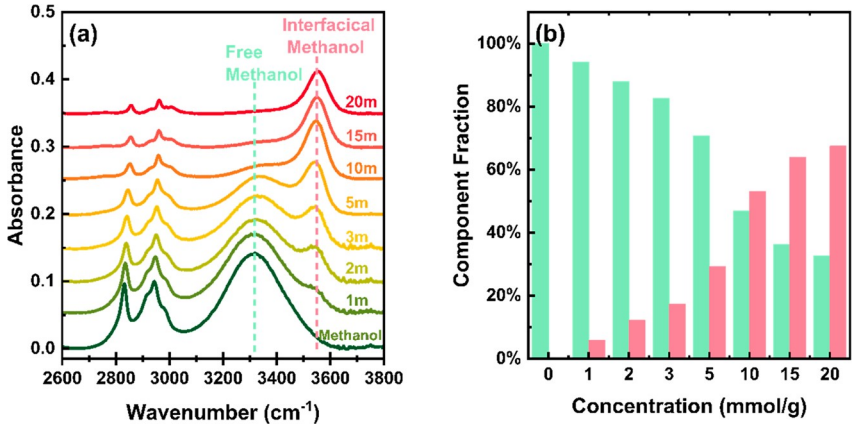

Figure 2. IR absorption spectra of the C−H and −OH stretch mode of methanol in LiTFSI's methanol solutions; (b) The alteration in the relative quantities, where interfacial methanol gradually became the major part with the concentration increase.

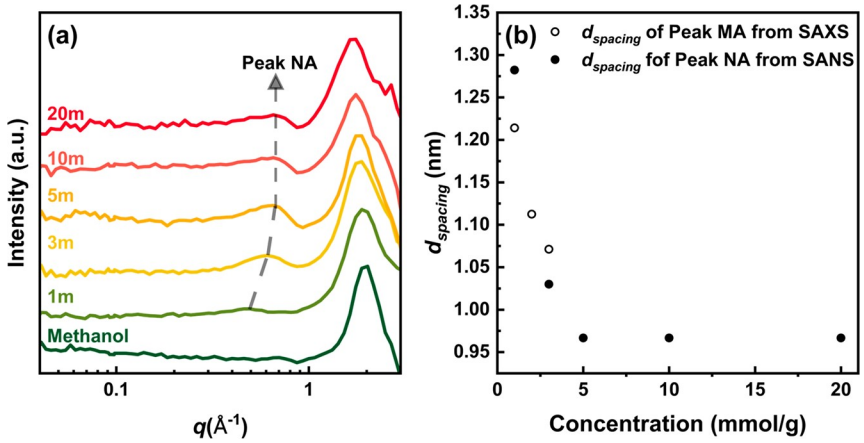

Figure 3. (a) SANS profiles for LiTFSI in deuterated methanol; (b) $d_{spacing}$ comparison between the peak NA and MA obtained from SANS and SAXS/WAXS, respectively.

could be calculated by the $d_{spacing} = \frac{2\pi}{q}$. The positions of peak MA and MB were accurately determined in the range 0.2 Å^{-1} ≤ q ≤ 1.3 Å^{-1}, after being subjected to Lorenz analysis (Figure S1 and Table S1). The $d_{spacing}$ of ASS and AN and the comparison with the water system is shown in Figure 1c. At the same concentration, the number of molecules of methanol is much smaller than the number of molecules of water. Therefore, LiTFSI's methanol solutions have a smaller $d_{spacing}$ of ASS than WISE. Meanwhile, the $d_{spacing}$ of AN in methanol is larger than that of water, because methanol has a larger molecular size (~0.41 nm[40]) than water (~0.28 nm[41]). Such results confirm that the second peak is not due to charge ordering but rather associated with the interfacial solvent trapped within the anion network.

We performed the FTIR study further to understand the influence of bulk and interfacial methanol. The FTIR spectra of OH stretching of methanol in LiTFSI's methanol solutions at different concentrations were obtained by the attenuated total reflection method (ATR) and displayed in the upper panel of Figure 2. The OH stretching frequency of pure methanol is centered at 3319 cm^{-1}. As the LiTFSI concentration increased from 1 to 20m, the intensity of the 3319 cm^{-1} IR band decreased while experiencing a blue shift. Hydrogen bonds can cause this alteration among the bulk methanol disrupted by the presence of LiTFSI.[9] Meanwhile, a new IR band positioned at 3547 cm^{-1} emerged and became dominated by the ascending of LiTFSI concentration. Referring to the WISE system, the new peaks were assigned to the interfacial methanol bonded with the $TFSI^-$ anion. The relative amount of the free methanol and interfacial methanol could be determined by the Gaussian analysis. As presented in Figure S2 and Table S2, at the concentration of 1m, the free methanol was the absolute major component, with interfacial methanol accounting for only 5.82%. As the LiTFSI concentration increased, an increasing amount of methanol disrupted the hydrogen bonds among themselves and instead became bound to $TFSI^-$. Interfacial methanol reached a maximum fraction of 67.42% when the concentration reached 20m.

To further investigate the behavior of methanol in solution, regular methanol was substituted with deuterated methanol (CD_3OD) to perform the small-angle neutron scattering (SANS). As shown in Figure 3, only one peak (peak NA) could be observed below q = 1 Å^{-1}, which is similar to those reported for the LiTFSI/D_2O system.[36,42] This peak was attributed to the CD_3OD−CD_3OD correlation. The peak is approximately located at q = 2 Å^{-1} and arises from the diffuse scattering of pure deuterated methanol. At lower concentrations (1−5m), this observable peak NA exhibits a similar behavior to peak MA in SAXS/WAXS. However, as the concentration increased (5−20m), peak NA and MA behavior diverged. In SAXS/WAXS, peak MA diminished and became unobservable, while peak NA remained detectable in SANS at

https://doi.org/10.1021/acsnano.3c10469
ACS Nano 2024, 18, 7037−7045

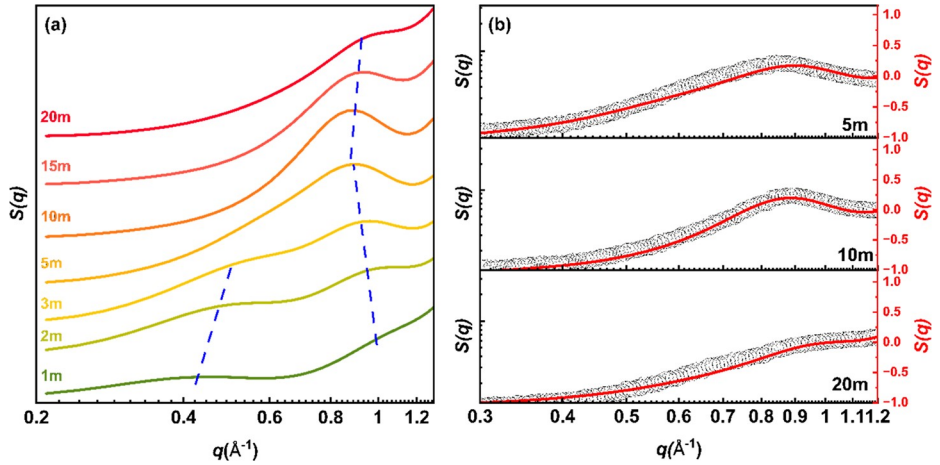

Figure 4. (a) X-ray scattering structure factor of various concentrations calculated from MD simulations with the GAFF force field; (b) Comparison of peak position from MD simulations (GAFF) (red) and experimental measurements for different concentrations (black).

approximately q = 0.65 Å^{-1} without any significant shift. The above phenomenon suggests that with the presence of the TFSI- anion, ordered deuterated methanol clusters were formed between ASS and AN. At lower concentrations, deuterated methanol clusters decrease in size as the concentration increases, aligning with the average distance with their corresponding ASS. This observation provides corroborative evidence within FTIR spectra that supports the proposition of hydrogen bond disruption between methanol due to the presence of $TFSI^-$ anions. Meanwhile, the unchanged peak position in higher concentrations means that irrespective of the relative concentrations of the anion solvated structure and anion network, the presence of free methanol is consistently observed.

We then performed MD simulations to provide a more profound understanding of the solvation structure. The structure factor ($S(q)$) of different concentrations obtained from MD simulations with two different force fields: general Amber force field (GAFF)[43] (Figure 4a) and optimized potentials for liquid simulations (OPLS-AA) (Figure S3a), and the computed radial distribution functions[44,45] were used to calculate the $S(q)$.[46−48] Both X-ray scattering $S(q)$ and neutron scattering $S(q)$ were computed from MD simulation to compare with experimental SAXS/WAXS and SANS data. The comparisons between the simulated X-ray $S(q)$ and experimental SAXS/WAXS results are presented. To facilitate a more convenient comparison, experimental $I(q)$ were converted to experimental $S(q)$ by dividing the SAXS/WAXS curve of 0.5m (Figure S4a), and a demo of this calculation is also shown in Figure S4b. From Figure 4b and Figure S3c, a comparison among experimental $S(q)$, GAFF, and OPLS-AA X-ray $S(q)$ is presented. Based on this comparison, we argue that the calculated $S(q)$ from GAFF seems to be more suitable for our SAXS/WAXS. Similar to the experimental SAXS/WAXS, peak MA from GAFF is only observed at lower concentrations of methanol (1, 2, and 3m), and the peak position shifts to higher q values with increasing concentrations. Peak MB is observed across all of the concentrations. The peak position of peak MB (GAFF) changes toward lower q values from 1 to 5m but changes toward higher q values from 10 to 20m, which agrees with the SAXS/WAXS experimental results. This finding indicates that among all of the characterization techniques, SAXS/WAXS is a more precise technology that could be used to validate the force field to MD.

The solvation structure is further represented by snapshots obtained from the MD simulations. The relationship among $TFSI^-$ anions (red), methanol molecules (blue), and Li^+ (green) in 1, 5, and 20m was selected to display in Figure 5a−c. As visualized in Figure 5a, the methanol molecules

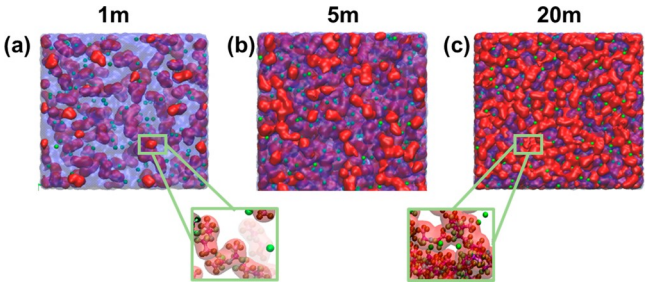

Figure 5. MD simulation snapshots of (a) 1, (b) 5, and (c) 20m. The red color presents the $TFSI^-$ anions, the green color presents the Li^+ ion, and the blue color presents the methanol molecules.

remain connected to each other in the most dilute solution, which confirms that bulk methanol is the main component. Upon zooming in for image display, the distances among $TFSI^-$ anions in the solution remain relatively sparse. When the concentration reaches 5m (Figure 5b), the large bulk of free methanol undergoes fragmentation due to the presentation of more $TFSI^-$ anions. Concurrently, the anion network is formed by the anion−anion interaction.[28] When the concentration reaches 20m (Figure 5c), the anion networks become the domain. Meanwhile, the magnified image reveals that the $TFSI^-$ anion forms a cluster instead of a single $TFSI^-$ anion.

To gain deeper insights into the evolution of $S(q)$, the decomposition of both X-ray scattering and neutron scattering $S(q)$ is also performed, and the results of 1, 5, 10, and 20m are plotted in Figure 6. The contribution of each type of solvent molecule/ion pair to the total $S(q)$ can be thoroughly examined in the decomposition plot. For the X-ray scattering $S(q)$ (shown in Figure 6(a−d)), peak MA and MB of the total $S(q)$ are contributed mainly by $TFSI^-$−$TFSI^-$, $TFSI^-$−methanol, and methanol−methanol, and only one peak (or

https://doi.org/10.1021/acsnano.3c10469
ACS Nano 2024, 18, 7037−7045

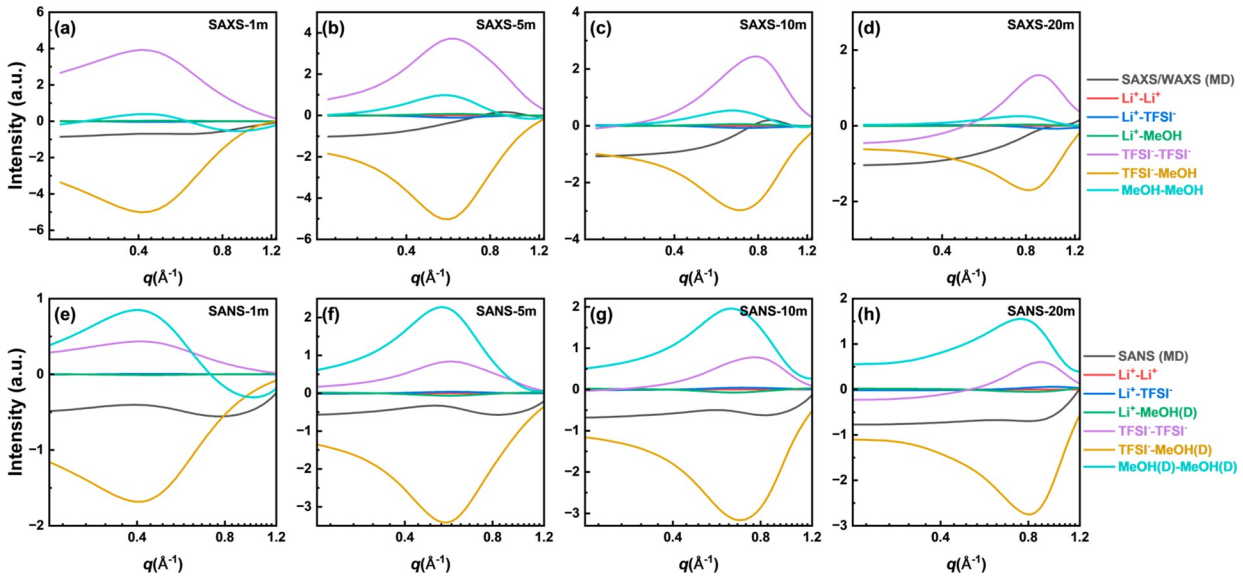

Figure 6. Decomposition of the simulated $S(q)$ from SAXS/WAXS of LiTFSI methanol solutions at (a) 1m, (b) 5m, (c) 10m, and (d) 20m, and decomposition of the simulated $S(q)$ from SANS of LiTFSI deuterated methanol solutions at (a) 1m, (b) 5m, (c) 10m, and (d) 20m.

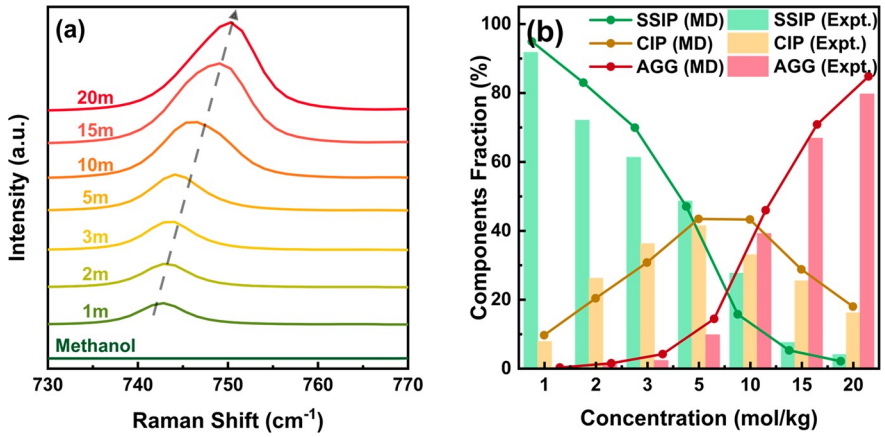

Figure 7. (a) Raman spectra of LiTFSI's methanol solutions with different concentrations; (b) anion coordination mode obtained from Raman (histogram) and MD with GAFF force field (scatter + line); green, yellow, and red present SSIP, CIP, and AGG, respectively.

antipeak) is observed for each of those species in the observed range of q. The peak positions of the decomposed $S(q)$ from $TFSI^-$−$TFSI^-$, $TFSI^-$−methanol, and methanol−methanol are mostly synchronized across all of the concentrations. However, the $TFSI^-$−$TFSI^-$ and methanol−methanol peaks are positive, while the $TFSI^-$−methanol peak is anticorrelated with the methanol−methanol and $TFSI^-$−$TFSI^-$ peaks. This phenomenon is also discovered in other electrolyte systems, i.e. water-in-salt,[6,36,49] which is interpreted as the alternations of anion−solvent−anion structure on the nanometer scale.[50,51] As the concentration of LiTFSI increases, the peak positions of the decomposed $S(q)$ from $TFSI^-$−$TFSI^-$, $TFSI^-$−methanol, and methanol−methanol move from lower to higher q. The decomposition of the neutron scattering $S(q)$ are shown in Figure 6(e−h). As we discussed for our experimental SANS results (Figure S5), only one major peak was observed in the low q region (peak NA), while the same phenomenon was also observed in MD calculated neutron scattering $S(q)$. Similar to the X-ray scattering $S(q)$, the neutron scattering $S(q)$ is also mainly contributed by $TFSI^-$−$TFSI^-$, $TFSI^-$−methanol, and methanol−methanol. However, the total $S(q)$ of peak NA is dominated by the methanol−methanol contribution in neutron scattering $S(q)$, while the X-ray scattering $S(q)$ is more dominated by the $TFSI^-$−$TFSI^-$ contribution.

With a full understanding of the global and local solvation structure related to methanol and $TFSI^-$ anions by SAXS/WAXS, SANS, and FTIR, the influence from concentration on anion coordination mode related to $TFSI^-$ anions and Li^+ cations was captured by Raman spectroscopy. As anticipated, the S−N−S bending vibration peak experienced both an increase in intensity and a blue shift as the $TFSI^-$ concentration rises (Figure 7a), which indicates more $TFSI^-$ anions and the transition of SSIP into CIP and AGG. The comprehensive breakdown of the information is visually represented in Figure S6 and listed in Table S3. To further substantiate the role of SAXS/WAXS in the validation of MD simulations, the anion coordination modes obtained from the GAFF and OPLS-AA force fields are depicted in Figure 7b and Figure S7 with experimental data for comparative analysis. SSIP (Experimental) decreased quickly from 91.81% to 4.11%, while SSIP (GAFF) showed the same trend from 90.43% to 2.06%. Meanwhile, both experimental and calculated CIP (GAFF) gradually increased from below 10% to nearly 40%, then decreased to approximately 17% simultaneously. As CIP

https://doi.org/10.1021/acsnano.3c10469
ACS Nano 2024, 18, 7037−7045

reaches its peak, a significant portion of SSIP and CIP convert to AGG, establishing AGG as the domain species within the solution. This transition phenomenon can be observed in both experimental data and MD (GAFF), and it is consistent between them. Just as calculated SAXS/WAXS is in better agreement with experimental data, SSIP obtained from OPLS-AA exhibits significantly greater deviations compared to GAFF at lower concentrations, and CIP derived from OPLS-AA is underestimated at low concentrations and overestimated at high concentrations. In contrast, a relatively better correspondence from OPLS-AA is observed with only with AGG.

CONCLUSION

The synchronal SAXS/WAXS reveals that the solvation structure change in different concentrations within the LiTFSI methanol solution is similar to that in the LiTFSI aqueous solution. The solvated structure only existed at a relatively low concentration, while the anion network was presented across the various concentrations. FTIR was able to indicate that the free methanol transits into interfacial methanol as the concentration increases. Meanwhile, SANS revealed the CD_3OD–CD_3OD correlations, which confirmed free methanol existed in the solution regardless of the concertation, which agrees with the outcome of FTIR. In addition to those, GAFF has been proven as the best force field for MD simulation to explain this proposed system. Further exploration based on simulated SAXS/WAXS decomposition as well as the solvation structures were examined extensively. Peak MA was mainly from the anion–anion and solvent–solvent contributions. The anion–anion interaction, in the meantime, was also the main contributor to peak MB. The above findings further confirmed that the high q peak around 1 $Å^{-1}$ (peak MB) is not from the charge ordering but from the anion network. More importantly, SSIP, CIP, and AGG obtained from MD simulation perfectly match the information from Raman analysis. This finding means that SAXS/WAXS could be utilized to provide strong validation for the force field of the MD simulation.

EXPERIMENTAL SECTION

Small-Angle X-ray Scattering/Wide-Angle X-ray Scattering. SAXS/WAXS experiments were conducted at the 12ID-B station of Advanced Photon Source at Argonne National Laboratory with an X-ray energy of 13.3 keV and a Pilatus 2M detector located about 2 m downstream from the sample. All samples, including the electrolytes and pure solvents, were loaded into the quartz capillary and sealed. The exposure time was 1 s, and all the measurements were performed at the room temperature. Experimental $S(q)$ values were obtained by dividing each concentration's curves by the curve corresponding to the lowest concentration (0.5m).

Small-Angle Neutron Scattering. The SANS measurements were performed at the GP-SANS (CG2), High Flux Isotope Reactor, Oak Ridge National Laboratory.[52] Two sample-to-detector distance/minimum wavelength, λ, settings were used to collect SANS data: 4 m with a minimum wavelength setting of 2.5 Å, and 1.3 m with a minimum wavelength setting of 2.5 Å, which provides a q range of ~0.04 $Å^{-1} < q <$ ~2.6 $Å^{-1}$, where $q = 4\pi \sin(\theta)/\lambda$ and 2θ is the scattering angle. The data reduction followed standard procedures using routines implemented in Mantid.[53]

Fourier-Transform Infrared Spectroscopy. FTIR experiments were carried out on a Shimadzu IRAffinity-1S spectrometer with a QATR 10 attachment. A droplet of samples was dropped on the sensor. Each sample was scanned 40 times and averaged. using the same method as the SAXS/WAXS. The laser wavelength applied for measurements is 532 nm, and the spectrum was scanned with a 2400 line/mm grating.

Molecular Dynamics Simulation. MD simulations were performed with a large-scale atomic/molecular massively parallel simulator (LAMMPS)[54] using the general Amber force field (GAFF).[43] The partial charge of the cations and anions was scaled to 0.6 of their original charges. The simulation details and force field parameters were included in the Supporting Information. Seven different concentrations (1, 2, 3, 5, 10, 15, and 20 m) were simulated, and each system's box size and number of ions are listed in Table S4. Each simulation consisted of two steps: an annealing run of 10 ns with canonical ensembles (NVT), and a production run of 40 ns with isothermal–isobaric (NPT) ensembles, where the first 20 ns of the NPT simulations were to equilibrate the simulation and the rest 20 ns were utilized to compute the properties. The temperature and pressure were controlled using Nose–Hoover thermostat and barostat.[55,56]

The equation below was used to compute X-ray scattering and neutron scattering $S(q)$

$$S(q) = \frac{\rho_0 \sum_i \sum_j x_i x_j f_i f_j \int_0^{L/2} 4\pi r^2 (g_{ij}(r) - 1) \frac{\sin qr}{qr} \frac{\sin(2\pi r/L)}{2\pi r/L} dr}{\sum_i x_i f_i^2}$$

where ρ_0, x_i, and x_j are the total number density, and atomic mole fraction of atom type i and j, respectively. $g_{ij}(r)$ is the radial distribution function between atoms of type i and atoms of type j. L is the length of the simulation box. f_i and f_j are either the form factors or the neutron scattering lengths. The form factors are used when calculating the X-ray $S(q)$ and the neutron scattering lengths are used when calculating the neutron scattering $S(q)$. The form factors are q dependent functions, and they are calculated using

$$f(q) = \sum_{i=1}^{4} a_i \exp\left(-b_i \left(\frac{q}{4\pi}\right)^2\right) + c$$

where the parameters a_i, b_i, and c are taken from Table 6.1.1.4 of Prince et al.[48] The neutron scattering lengths are constants taken from Sears et al.[57]

Raman Spectroscopy. Raman measurements were carried out on a Renishaw in-Via Raman Microscope. The samples were prepared

https://doi.org/10.1021/acsnano.3c10469
ACS Nano 2024, 18, 7037–7045

ASSOCIATED CONTENT

Data Availability Statement

Data can be obtained through contacting the corresponding authors upon reasonable requests.

Supporting Information

The Supporting Information is available free of charge at https://pubs.acs.org/doi/10.1021/acsnano.3c10469.

Peak positions and analysis results for SAXS/WAXS; analysis results for FTIR; comparison of peak position from MD simulations with OPLS force field and GAFF force field with experimental measurements for different concentrations; structure factor of various concentrations; neutron scattering of various concentrations calculated from MD simulations; Raman spectra and the fitting curves of LiTFSI methanol solutions; anion coordination mode obtained from Raman and MD with OPLS-AA force field, and GAFF force field (PDF)

AUTHOR INFORMATION

Corresponding Authors

Lei Cheng − *Materials Science Division, Argonne National Laboratory, Lemont, Illinois 60439, United States; Chemical Sciences Division, Oak Ridge National Laboratory, Oak Ridge, Tennessee 37831, United States;* orcid.org/0000-0002-3902-1680; Email: chengl@ornl.gov.

https://doi.org/10.1021/acsnano.3c10469
ACS Nano 2024, 18, 7037−7045

Tao Li − *Department of Chemistry and Biochemistry, Northern Illinois University, DeKalb, Illinois 60115, United States; X-ray Science Division, Argonne National Laboratory, Lemont, Illinois 60439, United States;* orcid.org/0000-0002-4913-4486; Email: taoli@anl.gov

Authors

Xingyi Lyu − *Department of Chemistry and Biochemistry, Northern Illinois University, DeKalb, Illinois 60115, United States;* orcid.org/0000-0002-5781-2486

Haimeng Wang − *Materials Science Division, Argonne National Laboratory, Lemont, Illinois 60439, United States*

Xinyi Liu − *Department of Chemistry and Biochemistry, Northern Illinois University, DeKalb, Illinois 60115, United States;* orcid.org/0000-0001-6092-2558

Lilin He − *Neutron Scattering Division, Oak Ridge National Laboratory, Oak Ridge, Tennessee 37831, United States*

Changwoo Do − *Neutron Scattering Division, Oak Ridge National Laboratory, Oak Ridge, Tennessee 37831, United States;* orcid.org/0000-0001-8358-8417

Soenke Seifert − *X-ray Science Division, Argonne National Laboratory, Lemont, Illinois 60439, United States*

Randall E. Winans − *X-ray Science Division, Argonne National Laboratory, Lemont, Illinois 60439, United States;* orcid.org/0000-0002-7080-7673

Complete contact information is available at: https://pubs.acs.org/10.1021/acsnano.3c10469

Author Contributions

[+]X. Lyu and H. Wang contributed equally.

Notes

The authors declare no competing financial interest.

ACKNOWLEDGMENTS

This work was supported as part of the Joint Center for Energy Storage Research, an Energy Innovation Hub funded by the U.S. Department of Energy, Office of Science, Basic Energy Sciences. Work performed at the Advanced Photon Source and the Center for Nanoscale Materials of Argonne National Laboratory, U.S. Department of Energy Office of Science User Facilities, was supported by the U.S. DOE, Office of Basic Energy Sciences, under Contract No. DE-AC02-06CH11357. A portion of this research used resources at the Spallation Neutron Source, a DOE Office of Science User Facility operated by the Oak Ridge National Laboratory. A part of this work was supported by Northern Illinois University's Molecular Analysis Core, which was established with support from Shimadzu Scientific Instruments. T. Li is thankful for the support from U.S. National Science Foundation (Grant No. 2208972, 2120559, and 2323117). We gratefully acknowledge the computing resources provided on Bebop, a high-performance computing cluster operated by the Laboratory Computing Resource Center at Argonne National Laboratory.

REFERENCES

(1) Jeon, J.; Lee, H.; Choi, J.-H.; Cho, M. Modeling and Simulation of Concentrated Aqueous Solutions of LiTFSI for Battery Applications. *J. Phys. Chem. C* 2020, *124* (22), 11790−11799.

(2) Yamada, Y.; Usui, K.; Sodeyama, K.; Ko, S.; Tateyama, Y.; Yamada, A. Hydrate-melt electrolytes for high-energy-density aqueous batteries. *Nature Energy* 2016, *1* (10), 16129.

(3) Suo, L.; Borodin, O.; Gao, T.; Olguin, M.; Ho, J.; Fan, X.; Luo, C.; Wang, C.; Xu, K. Water-in-salt" electrolyte enables high-voltage aqueous lithium-ion chemistries. *Science* 2015, *350* (6263), 938−943.

(4) Xu, Y.; Ding, T.; Sun, D.; Ji, X.; Zhou, X. Recent Advances in Electrolytes for Potassium-Ion Batteries. *Adv. Funct. Mater.* 2023, *33* (6), 2211290.

(5) Lv, T.; Suo, L. Water-in-salt widens the electrochemical stability window: Thermodynamic and kinetic factors. *Current Opinion in Electrochemistry* 2021, *29*, 100818.

(6) Zhang, Y.; Lewis, N. H. C.; Mars, J.; Wan, G.; Weadock, N. J.; Takacs, C. J.; Lukatskaya, M. R.; Steinruck, H.-G.; Toney, M. F.; Tokmakoff, A.; Maginn, E. J. Water-in-Salt LiTFSI Aqueous Electrolytes. 1. Liquid Structure from Combined Molecular Dynamics Simulation and Experimental Studies. *J. Phys. Chem. B* 2021, *125* (17), 4501−4513.

(7) Zhang, Y.; Maginn, E. J. Water-In-Salt LiTFSI Aqueous Electrolytes (2): Transport Properties and Li+ Dynamics Based on Molecular Dynamics Simulations. *J. Phys. Chem. B* 2021, *125* (48), 13246−13254.

(8) Qian, K.; Winans, R. E.; Li, T. Insights into the Nanostructure, Solvation, and Dynamics of Liquid Electrolytes through Small-Angle X-Ray Scattering. *Adv. Energy Mater.* 2021, *11* (4), 2002821.

(9) Zhang, M.; Hao, H.; Zhou, D.; Duan, Y.; Wang, Y.; Bian, H. Understanding the Microscopic Structure of a "Water-in-Salt" Lithium Ion Battery Electrolyte Probed with Ultrafast IR Spectroscopy. *J. Phys. Chem. C* 2020, *124* (16), 8594−8604.

(10) Miele, E.; Dose, W. M.; Manyakin, I.; Frosz, M. H.; Ruff, Z.; De Volder, M. F. L.; Grey, C. P.; Baumberg, J. J.; Euser, T. G. Hollow-core optical fibre sensors for operando Raman spectroscopy investigation of Li-ion battery liquid electrolytes. *Nat. Commun.* 2022, *13* (1), 1651.

(11) Du, Y.; Zhang, Z.; Xu, Y.; Bao, J.; Zhou, X. Metal sulfide-based potassium-ion battery anodes: storage mechanisms and synthesis strategies. *Acta Phys.-Chim. Sin* 2022, *38* (11), 2205017.

(12) Cabo-Fernandez, L.; Neale, A. R.; Braga, F.; Sazanovich, I. V.; Kostecki, R.; Hardwick, L. J. Kerr gated Raman spectroscopy of LiPF6 salt and LiPF6-based organic carbonate electrolyte for Li-ion batteries. *Phys. Chem. Chem. Phys.* 2019, *21* (43), 23833−23842.

(13) Walrafen, G. E. Raman Spectral Studies of the Effects of Temperature on Water and Electrolyte Solutions. *J. Chem. Phys.* 1966, *44* (4), 1546−1558.

(14) Gerlitz, A. I.; Diddens, D.; Grunebaum, M.; Heuer, A.; Winter, M.; Wiemhöfer, H.-D. Polypropylene carbonate-based electrolytes as model for a different approach towards improved ion transport properties for novel electrolytes. *Phys. Chem. Chem. Phys.* 2023, *25*, 4810.

(15) Suo, L.; Zheng, F.; Hu, Y.-S.; Chen, L. FT-Raman spectroscopy study of solvent-in-salt electrolytes*. *Chinese Physics B* 2016, *25* (1), 016101.

(16) Shen, Y.; Liu, B.; Liu, X.; Liu, J.; Ding, J.; Zhong, C.; Hu, W. Water-in-salt electrolyte for safe and high-energy aqueous battery. *Energy Storage Materials* 2021, *34*, 461−474.

(17) Xu, Y.; Yuan, Z.; Song, L.; Ding, T.; Sun, D.; Wang, L.; Zhou, X. Ultrathin Cobalt-Based Prussian Blue Analogue Nanosheet-Assembled Nanoboxes Interpenetrated with Carbon Nanotubes as a Fast Electron/Potassium-Ion Conductor for Superior Potassium Storage. *Nano Lett.* 2023, *23* (20), 9594−9601.

(18) Henderson, W. A.; Helm, M. L.; Seo, D. M.; Trulove, P. C.; De Long, H. C.; Borodin, O. Electrolyte Solvation and Ionic Association: VIII. Reassessing Raman Spectroscopic Studies of Ion Coordination for LiTFSI. *J. Electrochem. Soc.* 2022, *169* (6), 060515.

(19) Sudoh, T.; Shigenobu, K.; Dokko, K.; Watanabe, M.; Ueno, K. Li+ transference number and dynamic ion correlations in glyme-Li salt solvate ionic liquids diluted with molecular solvents. *Phys. Chem. Chem. Phys.* 2022, *24* (23), 14269−14276.

(20) Wang, L.; Uosaki, K.; Noguchi, H. Effect of Electrolyte Concentration on the Solvation Structure of Gold/LITFSI-DMSO Solution Interface. *J. Phys. Chem. C* 2020, *124* (23), 12381−12389.

(21) Lu, X.; Jiménez-Rioboó, R. J.; Leech, D.; Gutiérrez, M. C.; Ferrer, M. L.; del Monte, F. Aqueous-Eutectic-in-Salt Electrolytes for High-Energy-Density Supercapacitors with an Operational Temperature Window of 100 °C, from −35 to + 65 °C. *ACS Appl. Mater. Interfaces* 2020, *12* (26), 29181−29193.
(22) Lim, J.; Park, K.; Lee, H.; Kim, J.; Kwak, K.; Cho, M. Nanometric Water Channels in Water-in-Salt Lithium Ion Battery Electrolyte. *J. Am. Chem. Soc.* 2018, *140* (46), 15661−15667.
(23) Triolo, A.; Di Lisio, V.; Lo Celso, F.; Appetecchi, G. B.; Fazio, B.; Chater, P.; Martinelli, A.; Sciubba, F.; Russina, O. Liquid Structure of a Water-in-Salt Electrolyte with a Remarkably Asymmetric Anion. *J. Phys. Chem. B* 2021, *125* (45), 12500−12517.
(24) Li, T.; Senesi, A. J.; Lee, B. Small Angle X-ray Scattering for Nanoparticle Research. *Chem. Rev.* 2016, *116* (18), 11128−11180.
(25) Feng, Z.; Sarnello, E.; Li, T.; Cheng, L. Communication Microscopic View of the Ethylene Carbonate Based Lithium-Ion Battery Electrolyte by X-ray Scattering. *J. Electrochem. Soc.* 2019, *166* (2), A47.
(26) Liu, X.; Fang, L.; Lyu, X.; Winans, R. E.; Li, T. Unveiling the Liquid Electrolyte Solvation Structure by Small Angle X-ray Scattering. *Chem. Mater.* 2023, *35* (23), 9821−9832.
(27) Liu, X.; Yu, Z.; Sarnello, E.; Qian, K.; Seifert, S.; Winans, R. E.; Cheng, L.; Li, T. Microscopic Understanding of the Ionic Networks of "Water-in-Salt" Electrolytes. *Energy Material Advances* 2021, *2021*, 7368420.
(28) Yu, Z.; Curtiss, L. A.; Winans, R. E.; Zhang, Y.; Li, T.; Cheng, L. Asymmetric Composition of Ionic Aggregates and the Origin of High Correlated Transference Number in Water-in-Salt Electrolytes. *J. Phys. Chem. Lett.* 2020, *11* (4), 1276−1281.
(29) Shimizu, K.; Freitas, A. A.; Atkin, R.; Warr, G. G.; FitzGerald, P. A.; Doi, H.; Saito, S.; Ueno, K.; Umebayashi, Y.; Watanabe, M.; Canongia Lopes, J. N. Structural and aggregate analyses of (Li salt + glyme) mixtures: the complex nature of solvate ionic liquids. *Phys. Chem. Chem. Phys.* 2015, *17* (34), 22321−22335.
(30) Kashyap, H. K.; Hettige, J. J.; Annapureddy, H. V. R.; Margulis, C. J. SAXS anti-peaks reveal the length-scales of dual positive-negative and polar-apolar ordering in room-temperature ionic liquids. *Chem. Commun.* 2012, *48* (42), 5103−5105.
(31) Aguilera, L.; Xiong, S.; Scheers, J.; Matic, A. A structural study of LiTFSI-tetraglyme mixtures: From diluted solutions to solvated ionic liquids. *J. Mol. Liq.* 2015, *210*, 238−242.
(32) Liu, X.; Lee, S.-C.; Seifer, S.; Winans, R. E.; Cheng, L.; Z, Y.; Li, T. Insight into the nanostructure of "water in salt" solutions: A SAXS/WAXS study on imide-based lithium salts aqueous solutions. *Energy Storage Materials* 2022, *45*, 696−703.
(33) Lin, X.-S.; Wang, Z.-R.; Ge, L.-H.; Xu, J.-W.; Ma, W.-Q.; Ren, M.-M.; Liu, W.-L.; Yao, J.-S.; Zhang, C.-B. Electrolyte Modification for Long-Life Zn Ion Batteries: Achieved by Methanol Additive. *ChemElectroChem.* 2022, *9* (4), No. e202101724.
(34) Hao, J.; Yuan, L.; Ye, C.; Chao, D.; Davey, K.; Guo, Z.; Qiao, S.-Z. Boosting Zinc Electrode Reversibility in Aqueous Electrolytes by Using Low-Cost Antisolvents. *Angew. Chem., Int. Ed.* 2021, *60* (13), 7366−7375.
(35) Ma, L.; Vatamanu, J.; Hahn, N. T.; Pollard, T. P.; Borodin, O.; Petkov, V.; Schroeder, M. A.; Ren, Y.; Ding, M. S.; Luo, C.; Allen, J. L.; Wang, C.; Xu, K. Highly reversible Zn metal anode enabled by sustainable hydroxyl chemistry. *Proc. Natl. Acad. Sci. U. S. A.* 2022, *119* (24), No. e2121138119.
(36) Liu, X.; Lee, S.-C.; Seifert, S.; He, L.; Do, C.; Winans, R. E.; Kwon, G.; Z, Y.; Li, T. Revealing the Correlation between the Solvation Structures and the Transport Properties of Water-in-Salt Electrolytes. *Chem. Mater.* 2023, *35*, 2088.
(37) Qian, K.; Seifert, S.; Winans, R. E.; Li, T. Understanding Solvation Behavior of the Saturated Electrolytes with Small/Wide-Angle X-ray Scattering and Raman Spectroscopy. *Energy Fuels* 2021, *35* (23), 19849−19855.
(38) Liu, X.; Lee, S.-C.; Seifert, S.; Winans, R. E.; Z, Y.; Li, T. Relationship of the Molecular Structure and Transport Properties of Imide-Based Lithium Salts of "Acetonitrile/Water-in-Salt" Electrolytes. *Chem. Mater.* 2023, *35* (16), 6415−6422.
(39) Tomich, A. W.; Park, J.; Son, S.-B.; Kamphaus, E. P.; Lyu, X.; Dogan, F.; Carta, V.; Gim, J.; Li, T.; Cheng, L.; Lee, E.; Lavallo, V.; Johnson, C. S. A Carboranyl Electrolyte Enabling Highly Reversible Sodium Metal Anodes via a "Fluorine-Free" SEI. *Angew. Chem., Int. Ed.* 2022, *61* (51), No. e202208158.
(40) Takahara, S.; Kittaka, S.; Mori, T.; Kuroda, Y.; Takamuku, T.; Yamaguchi, T. Neutron Scattering and Dielectric Studies on Dynamics of Methanol and Ethanol Confined in MCM-41. *J. Phys. Chem. C* 2008, *112* (37), 14385−14393.
(41) Pashley, R. M.; Israelachvili, J. N. Molecular layering of water in thin films between mica surfaces and its relation to hydration forces. *J. Colloid Interface Sci.* 1984, *101* (2), 511−523.
(42) Horwitz, G.; Härk, E.; Steinberg, P. Y.; Cavalcanti, L. P.; Risse, S.; Corti, H. R. The Nanostructure of Water-in-Salt Electrolytes Revisited: Effect of the Anion Size. *ACS Nano* 2021, *15* (7), 11564−11572.
(43) Wang, J.; Wolf, R. M.; Caldwell, J. W.; Kollman, P. A.; Case, D. A. Development and testing of a general amber force field. *J. Comput. Chem.* 2004, *25* (9), 1157−1174.
(44) Loo, W. S.; Fang, C.; Balsara, N. P.; Wang, R. Uncovering Local Correlations in Polymer Electrolytes by X-ray Scattering and Molecular Dynamics Simulations. *Macromolecules* 2021, *54* (14), 6639−6648.
(45) Wu, F.; Roy, S.; Ivanov, A. S.; Gill, S. K.; Topsakal, M.; Dooryhee, E.; Abeykoon, M.; Kwon, G.; Gallington, L. C.; Halstenberg, P.; Layne, B.; Ishii, Y.; Mahurin, S. M.; Dai, S.; Bryantsev, V. S.; Margulis, C. J. Elucidating Ionic Correlations Beyond Simple Charge Alternation in Molten MgCl2-KCl Mixtures. *J. Phys. Chem. Lett.* 2019, *10* (24), 7603−7610.
(46) Liu, H.; Paddison, S. J. Direct calculation of the X-ray structure factor of ionic liquids. *Phys. Chem. Chem. Phys.* 2016, *18* (16), 11000−11007.
(47) Zhang, Y.; Lewis, N. H. C.; Mars, J.; Wan, G.; Weadock, N. J.; Takacs, C. J.; Lukatskaya, M. R.; Steinruck, H.-G.; Toney, M. F.; Tokmakoff, A.; Maginn, E. J. Correction to "Water-in-Salt LiTFSI Aqueous Electrolytes. 1. Liquid Structure from Combined Molecular Dynamics Simulation and Experimental Studies. *J. Phys. Chem. B* 2022, *126* (16), 3196−3197.
(48) Prince, E. *International Tables for Crystallography*, 3rd ed.; Wiley, 2004; Vol. *C*.
(49) González, M. A.; Akiba, H.; Borodin, O.; Cuello, G. J.; Hennet, L.; Kohara, S.; Maginn, E. J.; Mangin-Thro, L.; Yamamuro, O.; Zhang, Y.; Price, D. L.; Saboungi, M.-L. Structure of water-in-salt and water-in-bisalt electrolytes. *Phys. Chem. Chem. Phys.* 2022, *24* (18), 10727−10736.
(50) Dhattarwal, H. S.; Kashyap, H. K. Heterogeneity and Nanostructure of Superconcentrated LiTFSI-EmimTFSI Hybrid Aqueous Electrolytes: Beyond the 21 m Limit of Water-in-Salt Electrolyte. *J. Phys. Chem. B* 2022, *126* (28), 5291−5304.
(51) Saboungi, M.-L.; Borodin, O.; Price, D. L.; Farago, B.; González, M. A.; Kohara, S.; Mangin-Thro, L.; Wildes, A.; Yamamuro, O. Nanoscale structure of a hybrid aqueous-nonaqueous electrolyte. *J. Chem. Phys.* 2023, *158* (12). DOI: 10.1063/5.0138382
(52) Heller, W. T.; Cuneo, M.; Debeer-Schmitt, L.; Do, C.; He, L.; Heroux, L.; Littrell, K.; Pingali, S. V.; Qian, S.; Stanley, C.; Urban, V. S.; Wu, B.; Bras, W. The suite of small-angle neutron scattering instruments at Oak Ridge National LaboratoryThis article will form part of a virtual special issue on advanced neutron scattering instrumentation, marking the 50th anniversary of the journal. *J. Appl. Crystallogr.* 2018, *51* (2), 242−248.
(53) Heller, W. T.; Hetrick, J.; Bilheux, J.; Calvo, J. M. B.; Chen, W.-R.; DeBeer-Schmitt, L.; Do, C.; Doucet, M.; Fitzsimmons, M. R.; Godoy, W. F.; Granroth, G. E.; Hahn, S.; He, L.; Islam, F.; Lin, J.; Littrell, K. C.; McDonnell, M.; McGaha, J.; Peterson, P. F.; Pingali, S. V.; Qian, S.; Savici, A. T.; Shang, Y.; Stanley, C. B.; Urban, V. S.; Whitfield, R. E.; Zhang, C.; Zhou, W.; Billings, J. J.; Cuneo, M. J.; Leal, R. M. F.; Wang, T.; Wu, B. drtsans: The data reduction toolkit

https://doi.org/10.1021/acsnano.3c10469
ACS Nano 2024, 18, 7037−7045

for small-angle neutron scattering at Oak Ridge National Laboratory. *SoftwareX* 2022, *19*, 101101.
(54) Plimpton, S. Fast Parallel Algorithms for Short-Range Molecular Dynamics. *J. Comput. Phys.* 1995, *117* (1), 1−19.
(55) Hoover, W. G. Canonical dynamics: Equilibrium phase-space distributions. *Phys. Rev. A* 1985, *31* (3), 1695−1697.
(56) Shinoda, W.; Shiga, M.; Mikami, M. Rapid estimation of elastic constants by molecular dynamics simulation under constant stress. *Phys. Rev. B* 2004, *69* (13), 134103.
(57) Sears, V. F. Neutron scattering lengths and cross sections. *Neutron News* 1992, *3* (3), 26−37.

NOTE ADDED AFTER ASAP PUBLICATION

The version of this paper that was published ASAP February 19, 2024, contained an error in the instrumentation used for Small-Angle Neutron Scattering in the Experimental Section. The corrected version was reposted March 5, 2024.

https://doi.org/10.1021/acsnano.3c10469
ACS Nano 2024, 18, 7037−7045